Spacecraft Anomaly Forecasting Using Local Environment Data

Laila Andersson, Lars Eliasson, Olle Norberg

IRF Scientific Report 262

July 1999

ISSN 0284-1703

Institutet för rymdfysik

Swedish Institute of Space Physics

Kiruna, Sweden

Spacecraft Anomaly Forecasting Using Local Environment Data

Laila Andersson, Lars Eliasson, Olle Norberg

IRF Scientific Report 262

July 1999

Institutet för rymdfysik

Swedish Institute of Space Physics

Kiruna, Sweden

IRF Scientific Report 262
ISSN 0284-1703
ISBN 978-91-977255-9-0

Swedish Institute of Space Physics
Box 812
SE-981 28 Kiruna
SWEDEN
www.irf.se

STUDY OF PLASMA AND ENERGETIC ELECTRON ENVIRONMENT AND EFFECTS

ESTEC/Contract No. 11974/96/NL/JG(SC)

1999-07-16

TECHNICAL NOTE, WP 210

SPACECRAFT ANOMALY FORECASTING USING LOCAL ENVIRONMENT DATA

Authors
Laila Andersson, Lars Eliasson, Olle Norberg
Swedish Institute of Space Physics, Box 812, SE-981 28 Kiruna, Sweden

ESA Technical Officer:
A. Hilgers, Space Environments and Effects Analysis Section (TOS-EMA)
ESA Technological Research Programme Space Environments and Effects
Major Axis

Page left free intentionally

TABLE OF CONTENTS

Documentation Change Record

Issue	Rev.	Sect.	Date	Changes
Draft	0.1	All	970903	First draft for mid-term review
	0.2	All	980318	Version presented at PM5
	0.3	All	980428	Second draft sent to A Hilgers
	0.4	All	980518	Version presented at PM6
	1.0	All	980529	Version submitted to ESTEC for approval
	1.1	All	981207	Revised version
Final	1.2	All	990716	Second revision, mainly editorial

1 Introduction

1.1 Purpose of this study

This document is the final report of a study "Spacecraft anomaly forecasting using local environment data" (WP 210) that is a part of a subcontract performed under the contract "Study of plasma and energetic electron environment and effects."

The Meteosat spacecraft have experienced several anomalies at geostationary orbit. The first Meteosat spacecraft had unexpected anomalies (Hoge and Leverington, 1979) and therefore Meteosat-2 was equipped with SEM-1, an environmental monitor for electrons below 30 keV. The detected anomalies did not correlate with the changes in the low energy plasma (Coates et al., 1991). Therefore on Meteosat-3 another environmental detector SEM-2 (López Honrubia and Hilgers, 1996) was included on the spacecraft measuring higher energies. Rodgers and others at Mullard Space Science Laboratory and ESTEC have analysed the Meteosat data set in several case studies (see, e.g., Rodgers, 1991). A more detailed background to these studies is given in Section 2.5.

In this study the Meteosat-3 data set is used exclusively in order to analyse the effect of the local plasma environment on the spacecraft and the resulting anomalies. We have analysed the local environment data set and used it to predict the anomalies. We have also investigated the most important parameter determined from the local environment measurements on Meteosat-3 for prediction of the anomalies.

1.2 Spacecraft anomalies

The local plasma at the geostationary orbit (GEO) affects spacecraft and can cause anomalies. Anomaly is here defined as when a spacecraft changes its behaviour in a way that it was not designed for and is not caused by an operational error. This can be anything from a bit flip to a total malfunction of the spacecraft. In the early days of space activities, some anomalies on geostationary spacecraft were linked to the photoemission of the sunlit surfaces. With this knowledge new design recommendations for spacecraft were made. In plasmas where the local Debye length is larger than the spacecraft dimensions (such as in GEO) the recommendations are proper grounding of the satellite and use of conductive surface materials. These recommendations can minimise or prevent accumulation of charges that can generate a potential difference between the sunlit and the shaded side of the spacecraft (Frezet et al., 1989).

The geostationary orbit passes through the outer radiation belts with trapped electrons in the energy range 1 to 10 MeV. The electrons do not usually interact directly with electronic components because a modest amount of shielding (approximately 2 mm Al) is enough to stop the majority of them, although their accumulated dose can eventually cause significant component degradation. Electrons above 30 keV cause a large number of secondary particles, which in their turn can charge parts inside the spacecraft and cause deep-dielectric charging. Frederickson (1980) found that bulk charge in dielectrics required at least a week to decay and possibly much longer. Hence the effect of many bursts of energetic electrons can add up and cause problems on the spacecraft.

The time scale of charging depends on the capacitance of the surface as well as the magnitude of the charging current (Rodgers, 1991). In geostationary orbit, time scales for the charging of surfaces are in the order of seconds. The differential charging of the largest surfaces relative to each other may take from seconds to hours. Since periods of disturbed plasma likely to cause intense charging usually have time scales of minutes, equilibrium is not always reached. During eclipses, when of course photoelectron emission can not occur, the SEM-1 on Meteosat-2 frequently observed differential charging which caused potential differences of around -600 V in one hour. They disappeared minutes after the eclipse had ended. In GEO the shadowing of different surfaces has a strong influence on the spacecraft potential.
The accumulation of charges on a spacecraft depends on the charge transport (currents) to and from a surface (including charge transport in the structure). Low energy particles from the plasma are stopped on the surface (photoemission, ionospheric plasma), while high-energy particles penetrate the surface and can create secondary particles that can deposit charges somewhere else. Internal charging is caused by high-energy particles penetrating the spacecraft and depositing charges inside the spacecraft. Dielectric charging occurs when a potential has been built up in a dielectric material. Surface charging occurs on the surface of the spacecraft and interacts with the surrounding plasma. If one wants to monitor the low energy plasma surrounding the spacecraft these measurements will be affected by surface charging that can lead to either shielding or acceleration of low-energy charged particles.

Large potentials can be generated by the **v** x **B** force, depending, e.g., on the spacecraft size. Other sources are currents to and from the spacecraft such as photoelectron emission, auroral electron beams, and hot plasma injections during magnetic storms or auroral substorms. Charges do mainly accumulate at sharp edges. The amount of charging depends on the surface properties.

The accumulation of charges can reach a level such that electrical breakdown and powerful discharges occur. This can be between two points on the spacecraft or between the spacecraft and space. At a threshold, where the discharges occur, charges will move between the two points giving rise to a current, followed by an electromagnetic disturbance. This can cause an anomaly or damage the spacecraft. Light flashes, such as arcs on solar arrays (between interconnections and space) is a commonly observed discharge phenomena. In the Meteosat-1 ground tests small discharges on the spacecraft surface were observed as frequently as one discharge per second (Hoge, 1980). One problem with the discharges is that they can drain current from the spacecraft system and cause current spikes on the bus. The discharges do not only damage the electronics in different ways but they also damage parts (sputtering) and change the material properties. For dielectric charging the discharges can lead to changes of the dielectric properties. Discharges can lead to degradation, loss of solar strings, loss of electronic components and changed thermal properties. Discharges can cease after a period of time in space because of the changes they cause to the material.

Depending on energy and material properties, the radiation affects the material in different ways. Radiation can move atoms out of their lattice position and change the material properties. Radiation will mainly cause ageing of the material, change thermal and resistivity properties and cause darkening of glass etc. The effect will decrease the mission lifetime depending on the total dose to which the spacecraft is exposed. This effect is a long time effect. The material ageing continues until the end of the mission or until the part fails due to the high total dose of radiation. These environmental effects on the material have to be taken into account when designing the spacecraft.

High-energy particles penetrating material, such as silica, can cause charge production and accumulation in the material. This accumulation of charges can be large enough to cause malfunction of electronics. Single event effects (SEE) are described differently such as; bit flip, single event upset (SEU), latch up or single event burnout (SEB). This malfunction only needs one high-energy particle (usually MeV or higher). Protection from SEE by shielding is not trivial. The highest energy particles, those that can penetrate the shielding, can cause more secondary particles with a thicker shielding. If the flux of the energetic particles is constant during a mission the probability of a SEE is also constant. The design of the spacecraft has to be such that if a SEE occurs, the mission will not be at any risk. This could be from selection of components, redundant electronics or protective computer program routines.

Problems related to the local plasma environment have received special attention with the failure of the ANIK 1E (Baker et al., 1996) and the internal charging of Telstar 402 (Lanzerotti et al., 1996). The sister spacecraft Telstar 401 was lost during the large magnetic storm in January 1997 (Anselmo, 1997).

1.3 The space environment at geostationary orbit

To understand the occurrence of satellite anomalies at geostationary orbits (GEO) some basic knowledge of the plasma environment at GEO is needed. These orbits are circular at the geocentric distance of 6.6 R_E with low inclination; they are often referred to as geosynchronous orbits although the concept of geosynchronism is a wider concept. The plasma environment is controlled by the magnetic field configuration determined by the internal dipole field and external currents in the magnetosphere and the spacecraft move through variable plasma environments. The temporal variation of the solar wind influences the magnetosphere and the plasma characteristics at GEO. During magnetic storms the trapped particle belts inside GEO can grow in size and intensity, and more dense populations of particles (high energies) connected to the radiation belts will reach beyond the GEO and modify the spacecraft environment. The increase of particles in the radiation belts and the ring current comes mainly from the magnetosphere tail. Near and inside the GEO orbit electrons from the tail move eastward on trapped paths around the Earth. High-energy protons move in the opposite direction around the Earth. Particles that become trapped in the Earth's nearly dipolar magnetic field form a net westward ring current.

The main contributions to the ring current are particles in the keV energy range. The radiation belts consist mainly of particles with higher energies. The particles in the inner radiation belt are in stable trapped orbits, which implies that there is no obvious entry or sink for the inner radiation belt. The source is usually assumed to be galactic or anomalous cosmic rays (GCR or ACR). Since the loss rate is low the number density can grow to significant levels. As ACRs typically are only singly- or doubly-ionised they can reach lower parts of the radiation belt and play a significant role there compared to the more numerous GCR (Klecker, 1996). The decay of the radiation belts is slow and mainly caused by pitch angle diffusion and charge exchange with neutral particles.

During quiet times the geostationary orbit is always inside the magnetopause, but during severe magnetic storms the dayside magnetopause may move inside GEO. The plasma environment a spacecraft experiences depends on the local time. Because the majority of injections occur from the tail, the morning hours usually have bursty flows of electrons. At other local times the injected particles have been smeared out to lower concentration due to the adiabatic motion, energy filter effects and particle losses at the dayside magnetopause. High-energy electrons have the highest density in the noon sector due to the adiabatic motion and the compressed dayside magnetic fields. The typical plasma sheet electron temperature at GEO distance is 1 keV but during high geomagnetic activity the temperature can increase to 10 keV.

The angle between the Earth's magnetic dipole axis and the rotation axis is ≈11°. The geostationary orbit is in the plane of the Earth's rotation. Since the Earth is orbiting the Sun and the Earth's rotation axis is tilted with respect to the ecliptic plane, the geostationary orbit plane includes the Earth-Sun axis twice a year, during the equinoxes. The rest of the year the orbit is tilted compared to the Sun-Earth line. The solar activity follows an 11-year cycle. A 27-day periodicity in magnetic storms originates from the solar rotation. The 27-day rotation can clearly be seen in the high-speed solar wind streamers during the declining phase of the solar cycle.

The sun is more active during solar maximum. The last solar maximum occurred in July 1989. A coronal mass ejection (CME) which reaches the Earth is often linked with strong magnetic storms and great auroras. The solar proton events are associated with these CME. During solar minimum more cosmic rays can penetrate into the solar system and reach the Earth's inner magnetosphere. At maximum the solar magnetic field can shield the inner solar system from the lower end of the high-energy galactic cosmic rays.

2 Data and earlier studies

2.1 Meteosat

The first Meteosat satellite, Meteosat-1, was launched in November 1977. The satellite was a spin-stabilised meteorological satellite with the main payload consisting of a scanning radiometer. The satellite recorded several anomalies. Since Meteosat-2 was already planned, a first investigation of the effects was made after only one year (Hoge and Leverington, 1979) to give guidelines for Meteosat-2. Clear correlation between anomalies and the spring equinox and a smaller correlation with the autumn equinox were seen for four satellites; Skynet, Meteosat-1, Symphonies-A and B. Correlation with local time, solar direction and eclipses could not be established. A clear correlation between anomalies on Meteosat-1 and the geomagnetic index two days before the detected anomaly was seen (the two day delay was also indicated in the Skynet data). A ground test of the engineering model was set up for investigation of the space environment effects on Meteosat-1. On Meteosat-1 about 80% of the outer surface was not conductive (e.g. solar cell cover glass, second surface mirrors and black paint) and large metallic surfaces of the thermal shields were not grounded, because no cost-effective solution existed at the time of construction. The grounding system on Meteosat-1 was a multi-point grounding system. A current injection test did not lead to any failures during the five weeks of ground testing. Thermal shield test of irradiation was performed but the discharges were smaller than expected and seemed to have no impact on the satellite. The result from an electron irradiation test (Hoge and Leverington, 1979; Hoge, 1980 and Hoge, 1982) showed that virtually all isolated surfaces on Meteosat-1 were subject to arc discharges every second or so but the energy was too low to cause any damage. The test was set up to produce the same conditions as for a substorm.

From the Meteosat-1 spacecraft charging investigation the recommendation for the design of Meteosat-2 was to ground the shield, improve the critical interfaces and incorporate charging monitors. The charging monitors on Meteosat-2 consist of an electron analyser, SSJ3, built at Emmanual College, Boston, USA and an electrostatic-discharge monitor EEM-1 built at ESA/ESTEC. The SSJ3 had an energy range of 50 eV-20 keV in a low and a high energy channel. The Mullard Space Science Laboratory processed the data.

The Meteosat-2 with the improved design was launched in June 1981. Meteosat-2 also encountered anomalous status changes (Hoge, 1982). During the first year a good correlation of Meteosat-2 flux measurements and the Marecs-A satellite anomalies was observed (Hoge, 1982). Most of the Marecs-A anomalies occurred when the spacecraft passed through the plasma sheet. The interest of looking at more energetic radiation was raised. From the Meteosat-2 satellite the rapid degradation of the solar array indicated the existence of high-energy particles but it did not correlate with the anomalies (Hoge, 1982). Coates et al. (1991) studied almost six years of anomalies from Meteosat-2 and found that the anomalies did not fit the pattern for surface charging effects and no real link was found. They suggested deep dielectric charging as the most likely explanation.

Hoge (1982) concluded that the improvement of the design on Meteosat-2 was effective although the monitor data did not agree with the hypothesis for the charging mechanism leading to these modifications. Other types of environmental effects or on-board generated interference may have been the cause of the remaining Meteosat-2 “arcing” anomalies. A spectrum of monitors for future launches was recommended.

For Meteosat-3 a new environmental monitoring instrument SEM-2 was used to measure higher energies. The SEM-2 was built at the Mullard Space Science Laboratory, UK, under contract to ESA/ESTEC.

An assessment study (Frezet et al., 1989) was made on GEO satellites, one of which was Meteosat-2. The NASCAP and MATCHG codes were used to investigate electrostatic charging, especially for the radiometer cavity on Meteosat-2. To investigate seasonal dependence the code was run for different solar aspect angles. Less charging was found at solstice conditions than at equinoxes because of the larger sunlit area. The study recommended avoiding floating metalisation and high-resistivity material. The differential charging was reduced considerably when all conductors were grounded. Further improvements were seen when insulation black paint was made conductive and the Teflon was replaced by the lower-resistivity Kapton. With this the charging of the cavity was almost removed. In the result of the test a seasonal dependence was observed but a good correlation between severe plasma events and the observed Meteosat anomalies was lacking. This indicated that at least part of the problem was caused by "deep-dielectric charging" induced by high-energy electrons.

2.2 Meteosat-3 orbit and operational period

Meteosat-3 was launched on 15 June 1988, to become one of ESA's geostationary satellites in the meteorological satellite series. Eumetsat operated the satellite. During the lifetime of Meteosat-3 the satellite was moved several times (see Table 1).

Table 1. *Meteosat-3 positions*

From	To	Position
Launch 15 June 1988	June 1989	0°E
June 1989	January 1990	50°W
January 1990	April 1990	0°E
April 1990	November 1990	5°W
July 1991		50°W
late 1992		75°W
April 1993		72.8°W
February 1995	November 1995	70°W, inclined

In May 1995 Eumetsat decided that it did not need the satellite back in position so it was kept in reserve around 70°W before final burn. Meteosat-3 was put into junk orbit on 21 November 1995.

The anomaly set covers the full time period, i.e. from 21 June 1988 to 20 October 1995. The environmental monitor SEM-2 operated during the same time period except for a few months (see Section 2.4).

2.3 Types of anomalies on Meteosat-3

Meteosat-3 had many different types of anomalies. In Table 2 the anomalies are presented in 18 different categories. The most common anomaly is on the radiometer, 70% of all anomalies. The radiometer is placed in the central part of the satellite. The total number of anomalies during the operational lifetime of the satellite was 724. The anomalies are well spread over the full orbit coverage as shown in Figure 1.

Table 2. *Codes of Meteosat-3 anomalies*

Code	Description	Nr of anomalies
1	Radiometer stops	295
2	Radiometer position jump	84
3	Radiometer position jump and stop	127
4	Other radiometer anomalies	3
5	Battery charger 1 anomaly	7
6	Battery charger 2 anomaly	49
7	Battery charger 1 and/or 2 off	14
8	Battery charger rate anomaly	4
9	Digital multiplexer 1 off / 2 on	8
10	Corrupted/lost image lines	67
11	Command decoder anomaly	3
12	Temperature reading anomaly	14
13	SIC anomaly	29
14	EDA bias jump, SIC lid jump, rad gain	5
15	VIS 2 gain jump	2
16	Regulator loop voltage anomaly	2
17	Spurious memory reconfiguration	2
18	Other anomalies	9

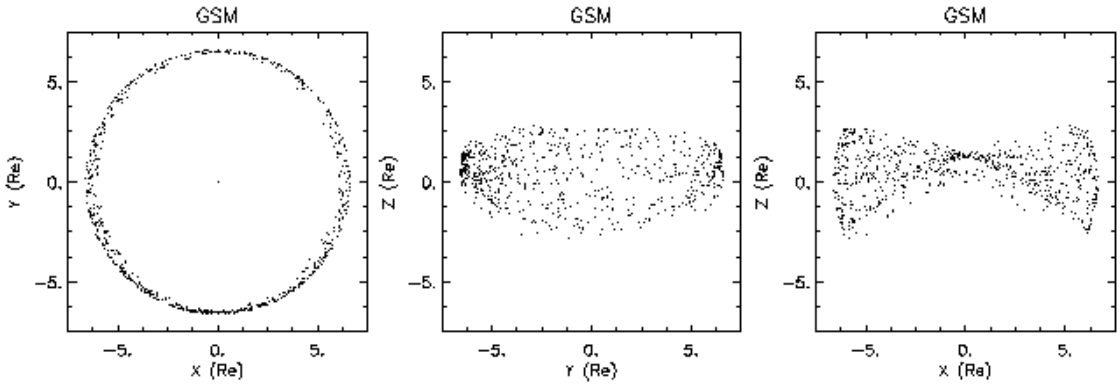

Fig 1. *The location of the anomalies in the orbit, plotted in GSM coordinates.*

2.4 Meteosat-3 environmental data set

The space environment monitor on Meteosat-3, SEM 2, covers the energy range 42.9-300 keV (Table 3) with a time resolution 8-10 minutes (Rodgers, 1991). The SEM-2 has low mass (2.5 kg), power (1.8 W) and telemetry rate (1.9 bits/s), which meant that the instrument did not have any significant impact on the main function of the spacecraft. The energy range was selected to look for deep-dielectric charging effects. It was based on an array of five surface barrier detector-collimator systems and was built by the Los Alamos National Laboratory and recalibrated by Mullard Space Science Laboratory. The detectors were arranged in a fan with each set at a different angle to the spacecraft spin axis to give five polar angle bins. The field of view of each detector was 5 degrees. Azimuth information was obtained by the spacecraft motion. The spin axis was aligned with the Earth's north-south axis. It is a solid-state detector that uses the stop length to estimate the energy. The highest energy bin includes all high-energy particles, as well as those that do not stop in the detector (energies above 300 keV).

Table 3. *The energy bins of SEM-2*

Energy Bin	**E_{lower}**	**E_{upper}**
1	201.8 keV	300 keV
2	134.9 keV	201.8 keV
3	90.7 keV	134.9 keV
4	59.4 keV	90.7 keV
5	42.9 keV	59.4 keV

An anisotropy index was derived from a two-dimensional array of fluxes at each polar and azimuth angle range, summed over all energy bins. This index was calculated by fitting spherical harmonics to the data (Rodgers, 1991 and references therein). Zero second-order anisotropy indexes correspond to an isotropic distribution. Negative index corresponds to an equatorial enhanced or "pancake" distribution that is frequently seen near local midnight where most electrons in this energy range have come from the tail. The axis of symmetry of the distribution is found in the same fitting process and is expressed in terms of its polar angle, θ, and azimuth angles, ϕ. Since the electrons are theoretically organised by the magnetic field, the axis of symmetry is an indicator of the magnetic field direction, although the sign and strength of the magnetic field is still unknown.

The data files available for this study were stored in two data sets with the resolution 8-10 min and 30 min respectively. Only the 30-minute resolution data set was used. The SEM-2 data files contain: flux (summed over ϕ and θ) as function of energy, flux (summed over energy and ϕ) as function of θ, flux (summed over energy and θ) as function of ϕ, flux (summed over energy) as function of ϕ and θ, total flux (summed over energy), spectral index (γ), second-order anisotropy index α, and the polar (θ) and azimuth (ϕ) angles defining the axis of symmetry, K_p (the planetary magnetosphere activity index) and the status of the on-board memory SEU monitor.

At the beginning of the mission there are more sporadic electron fluxes (solar maximum, while at the end (solar minimum) there are more regular changes due to the 27-day rotation of the sun (Figure 2). There is a variation between the daily average fluxes but no clear changes of the mean flux between solar minimum and solar maximum. The variation during one day is much larger than variation from day to day (Figure 3).

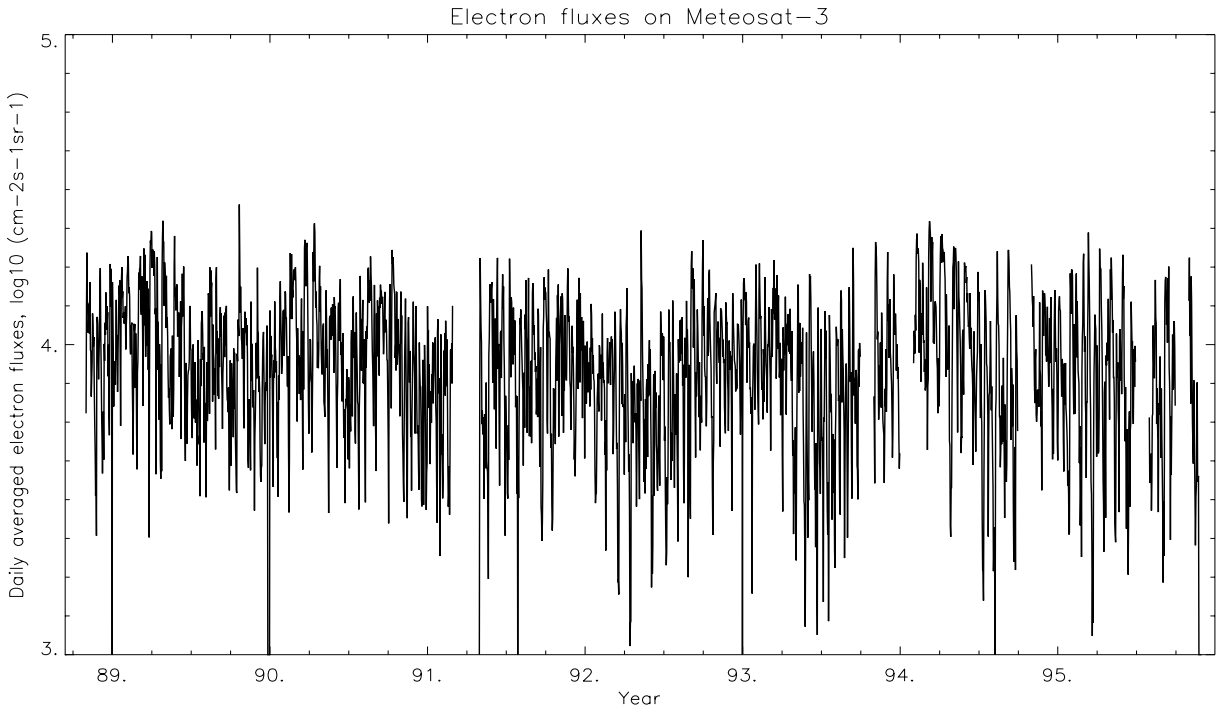

Fig 2. *Daily average fluxes measured by SEM-2. The time series has 6 longer time gaps.*

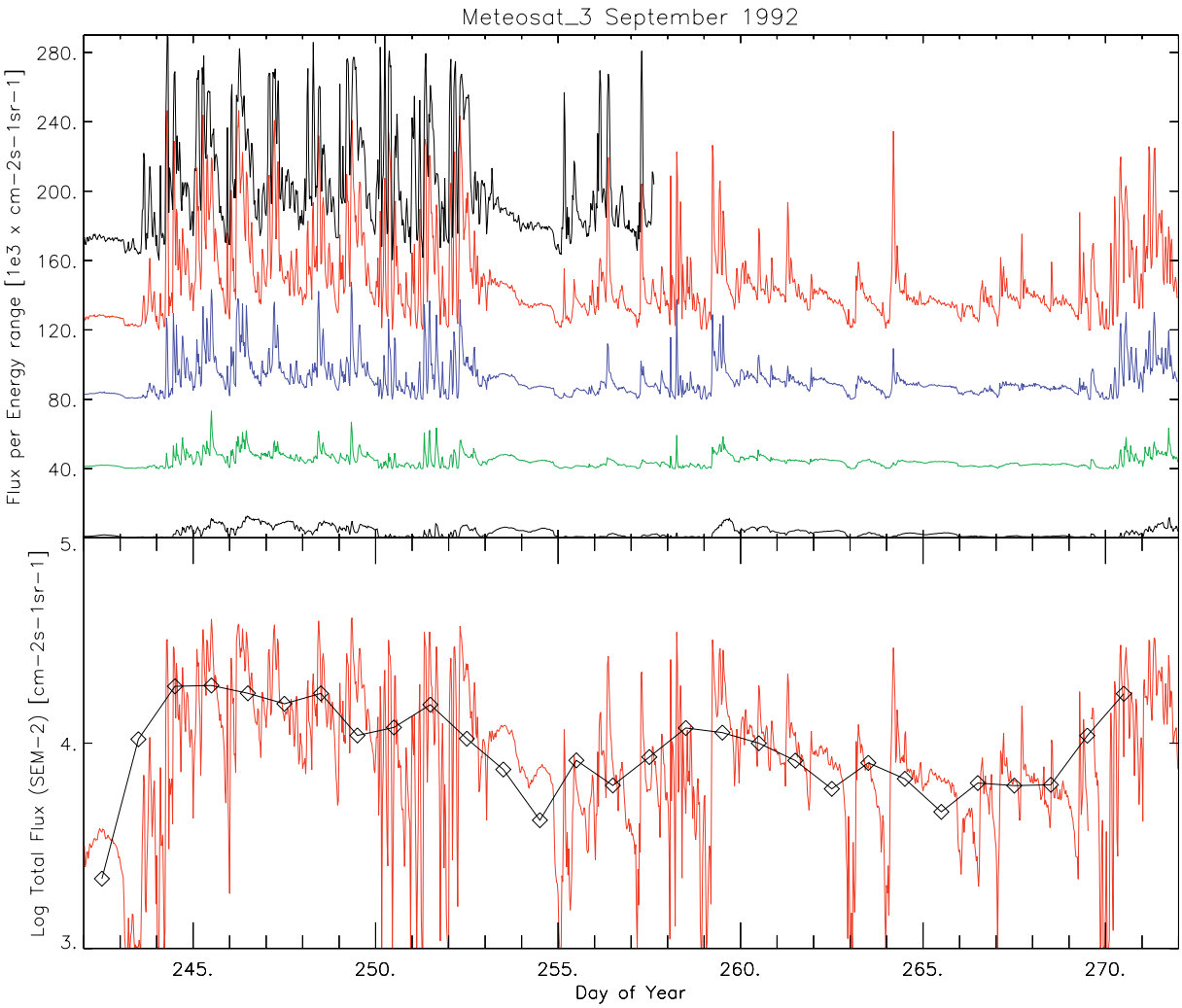

Fig 3. *Electron fluxes from SEM-2 at September 1992. The top panel shows fluxes (linear scale) for the five energy bins. The energy bins are shifted 4000 ($cm^{-2}s^{-1}sr^{-1}$), starting with bin 0 at the bottom (high energy). The bottom panel shows the total flux with 30 min and 24 hour time resolution, respectively.*

2.5 Earlier studies predicting Meteosat-3 anomalies

A number of investigations have used the Meteosat-3 (also called Meteosat P2) environment data set. Here follows a short description of some of them and their conclusions.

Rodgers (1991) studied 166 anomalies from the radiometer together with primarily the low-resolution data from SEM-2. A clear correlation was seen between some of the anomalies and the electron flux. A statistical study showed that for a typical anomaly the flux levels had been built up during the preceding 80 hours. Anomalies correlated with the highest fluxes occur mainly at 3-9 local time (LT). Anomalies correlating with low fluxes and longer build up times occur at 15-24 LT. Both seem to be more correlated with the high energy range on

SEM-2 and indicate that deep-dielectric charging is the most likely cause. Different energy ranges and their relative importance were compared using a time window around the anomaly and an average level (not time dependent). No correlation was found with incident angle for low-resolution data but for high resolution some dependency of theta was discovered. Earlier studies showed that anomalies have a strong seasonal dependence. This suggested that eclipse periods are important. The equinox coincides with the sun shining directly into the radiometer cavity, and this should reduce the surface charging effect but would not effect the deep-dielectric charging effect. Rodgers (1991) concluded that the anomalies might have different causes but are probably due to deep-dielectric charging. The morning anomalies seemed to be triggered by a high flux of particles while evening anomalies had a long accumulation phase, over 8 days without a peak in the fluxes.

Rodgers et al. (1999) continued the earlier study of Meteosat P2 anomalies now with the full seven-year anomaly data set (total 725 anomalies) together with the SEM-2 data. The detailed investigation was only on the radiometer anomalies (486 anomalies). They found that the highest energy channel was correlated with anomalies with high fluxes at the time of the anomaly. The 5-9 LT anomalies are mostly correlated with the high-energy channel. These were again suggested to result from deep-dielectric charging, and 16 of 121 anomalies in 5-9 LT occurred in the same 3-hour bin as the previous anomaly. The other, especially 17-21 LT, anomalies occurred after long build-up times and with relatively low fluxes at the time of the anomaly.

López Honrubia and Hilgers (1997) investigated the application of pattern classification techniques to anomaly data analysis. They used 40 anomalies over 5 years from Meteosat-3, 4, and 5 (also known as Meteosat P2, launched 1988, and Meteosat Operational Satellites MOP-1, mid 1989 and MOP-2, February 1994) together with high energy (>2 MeV) electron measurements from the US series of Geostationary Operational Environmental Satellites (GOES). The data set was divided into two classes “anomaly” and “non-anomaly”. The analysis was made with a Learning Vector Quantization (LVQ) network. The data set contained 2000 input vectors, 40 of which were associated with anomaly days. The training of the network took into account that there are few anomalies compared with non-anomalies. The input data consisted of an N-day window with N-days of the mean daily flux; the window did not use information from the same day as the anomaly to make the analysis to be a prediction. The output was 1 if there was an anomaly the following day, -1 if there was an anomaly within the window N before or after and otherwise 0 (the cases with -1 were not analysed). Although limited by the small amount of anomaly data the technique allowed to give evidence of correlation of this type of anomaly with MeV data measured by the GOES spacecraft and of time dependent effects.

Grystad (1997) applied similar technique as López Honrubia and Hilgers (1997) to analyse P2 anomaly and environment data. Both a Bayesian linear classifier and an LVQ were used on the Meteosat -3 anomaly set and on the on-board SEM-2 instrument. The highest energy channels showed slightly different characteristics with a maximum at 4 days. The main conclusions, although still preliminary, were that the lower energy range correlates when only average flux over the latest day is considered, while for higher energies the best window length is longer, using both network methods.

3 Anomaly occurrence frequencies and locations

3.1 Local time and seasonal dependence

In Figure 4 all anomalies from Meteosat-3 are presented as number of anomalies vs. the local time. It can be seen that more anomalies occur in the late evening/early morning sector (00-09 LT) than during the rest of the day. This has also been seen in earlier studies (Wilkinson, 1994; Vampola, 1994 and Wrenn and Sims, 1993). The increase of anomalies is usually attributed to the more frequent injection and drift of electrons into this sector.

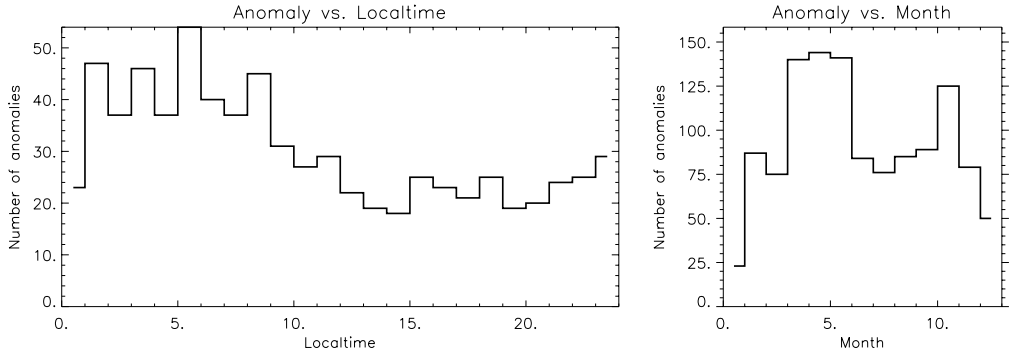

Fig 4. *Meteosat-3 anomalies vs. the local time and month, respectively.*

The radiometer anomalies have a peak in the midnight - morning sector (Figure 5). The battery charger anomalies are clearly correlated with equinox times. An interesting observation is that almost all battery anomalies occur when the z-coordinate is positive. The image line anomalies occur late in the mission and could be due to ageing or cosmic rays. The SIC have a tendency to peak at noon and could be a charge accumulation effect. The rest of the anomalies are evenly spread over the year and local times. Again, as for the battery charger anomaly, these anomalies seem to be more frequent at positive z-axis. The effect of the special conditions during equinox is clear on most types of the anomalies.

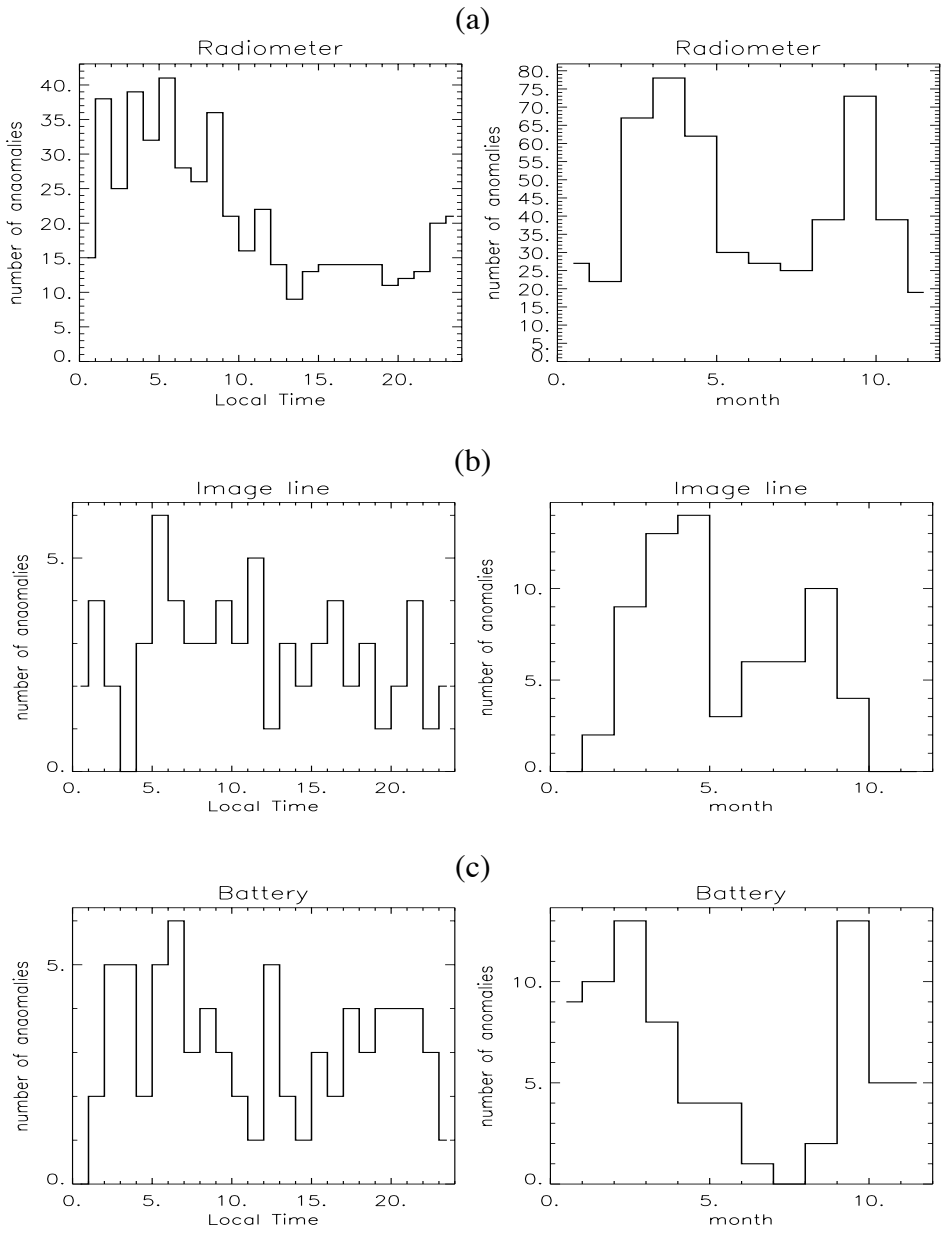

Fig 5. *Different anomalies plotted vs. local time and month. The different figures show; a) Radiometer anomalies (code 1, 2, 3, 4); b) Image line anomalies (code 10) and c) Battery anomalies (code 5, 6, 7, 8).*

3.2 Solar cycle and life-time dependence

The solar cycle dependence is difficult to analyse because the operational period of the satellite covers less than one solar cycle. More anomalies occur at the end of the mission.
The mission started during solar maximum (1989) and continued into solar minimum. If the effect is mainly due to coronal mass ejections (CME), the number of anomalies should be highest in the beginning of the mission (closer to solar maximum). If the anomalies are mainly affected by radiation it could be either solar proton events (solar maximum) or GCR and ACR, in which case the satellite should be affected mainly at solar minimum. The ageing of the spacecraft should in most cases increase the occurrence of anomalies with time, but for some cases the ageing can cause anomalies to disappear. In this study we can not separate the ageing effect from the solar cycle effect.

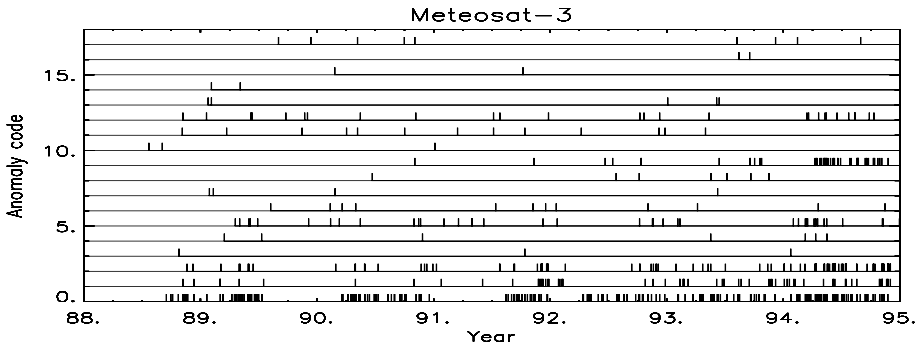

Fig 6. *The different anomalies as function of time (for codes see Table 2).*

4 Use of neural network for anomaly prediction

4.1 Principal component analysis

We selected an integration time of two hours. For each energy bin the average flux was calculated. In addition, for each interval the maximum and minimum values were saved. A fourth value was calculated for the interval, a "running mean" to represent long time effects. This "running mean" value was selected to be an average value of the previous 72 hours. This length of the time window was selected because it is longer than a day (to average out daily variations) and less than the effects of a magnetospheric storm (see Section 1.3).

A data file consisting of a time series of average fluxes from all five energies with a resolution of two hours (represented as rows in the data files) was set up. Also, as discussed above, the maximum and minimum value during the time interval and the running mean value were added for each energy bin. This led to twenty values (representing the columns in the data file). In addition four more values were added until the data file consisted of 24 columns. The added values were the spectral index, anisotropy index, theta and phi (see Section 2.4 for a description). This data set is referred to as "_all" throughout the report.

Two other data files were created, consisting of information from only three energy bins (four x three = twelve columns). They will be referred to as "_high" for the file containing information from energy bin 1, 2 and 3 (the highest energies) and "_low" for the energies 3, 4, and 5 (the lowest energies). (Note: Tests have also been made using the two lowest and the two highest energy levels. These tests gave the same result as using 3 levels.

During the lifetime of Meteosat-3 there were six periods, one month or longer, when SEM-2 was not operated, Figure 3. As a result the data set had to be treated as seven separate time series. A few small gaps (4 hours or less) were detected and replaced with a linear interpolation from the points surrounding the data gap.

"_all" is a data set with 27 dimensions. Principal component analysis (PCA) can be used to transform a large-dimensional data set to three coordinates represented as the coordinates with the largest variance in the data set (see Appendix). To get the eigenvalues of the PCA the second period of continuous measurements was selected. These eigenvalues were then used on all seven-time periods; i.e. the coordinate transformation is the same for all time periods. The calculated eigenvalues (Figure 7) can be seen as the constants of a linear transformation from many dimensions to three. In Figure 7 the variance is largest in PCA1, representing the instantaneous particle flux. The second largest, PCA2, is the long time fluxes, and the third, PCA3, the spectral-slope index. Figure 7 shows these values.

In Figure 8 the PCA1 is plotted together with anomalies. In PCA1 periods of smooth data can be seen (e.g., day 25). Sometimes the time series are interrupted by a periodicity of 12 points (one day) which can be a signature of an injection into GEO (e.g., day 145). By eye it seems that an anomaly is often preceded by these interruptions one to two days before. At other times the time series is fairly variable. At these periods the time series rise in value and frequently a number of anomalies are detected afterward (e.g., day 82).

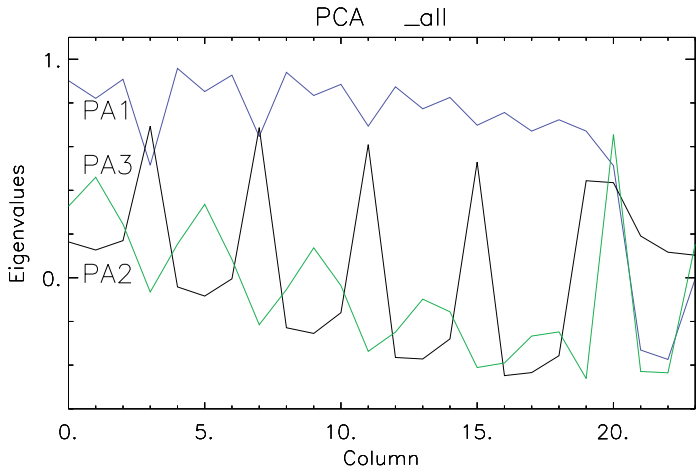

Fig 7. *The result after Principal Component Analysis of the electron fluxes of SEM-2. The eigenvalues of the three first components vs. the input values (columns) are described in the text.*

The PCA analysis is made separately for the three data sets (_all, _high and _low). The second continuous time period is used to calculate the PCA and the calculated eigenvalues are used on all seven time periods.

4.2 Using the time history and dynamics

The goal of this study is to find a possible way of predicting anomalies from the local measurements. The local measurements have been transformed into three values representing PCA1, 2, and 3. A data set with a time window preceding the time of prediction of an anomaly (1) or non-anomaly (0) was created. The time window was constructed using only every 12th point from the original data, i.e., using the measurement at the time of prediction together with data 24 and 48 hours before the time of interest, thus making the time window width 2 days. This leads to a data set consisting of 3 x 3 columns where the PCAs are shifted 0, 12 and 24 points with respect to each other. The example described above is referred to as pa3. Other combinations of PCA are described in Table 4.

As discussed in Section 4.1 the dynamics in PCA1 reveal a lot of information. Therefore a frequency analysis was performed. In order only to use data before the time of interest, a frequency analysis has to be done for each two-hour interval. The frequency analysis is performed in a window where the last point in the window represents the point where the prediction is made. For each point (time step) the window has to be shifted one step and a new analysis be made. Previous studies indicate that the time window should be 10 days or less. The window for the frequency analysis was therefore selected to be 128 points or less. One can use Fourier analysis to calculate the frequency but in this study we used a wavelet transformation (Kumar and Foufoula-Georgiou, 1997).

The wavelet analysis was performed on the strongest component, PCA1, after the data was low-pass filtered. The wavelet transformation was a 15 point. The tested time windows are 32, 64 and 128 points and throughout the report they will be referred to as wa32, wa64 and wa128, respectively. The frequency analysis was made for all three sets (i.e. for "_all", "_high" and "_low") separately.

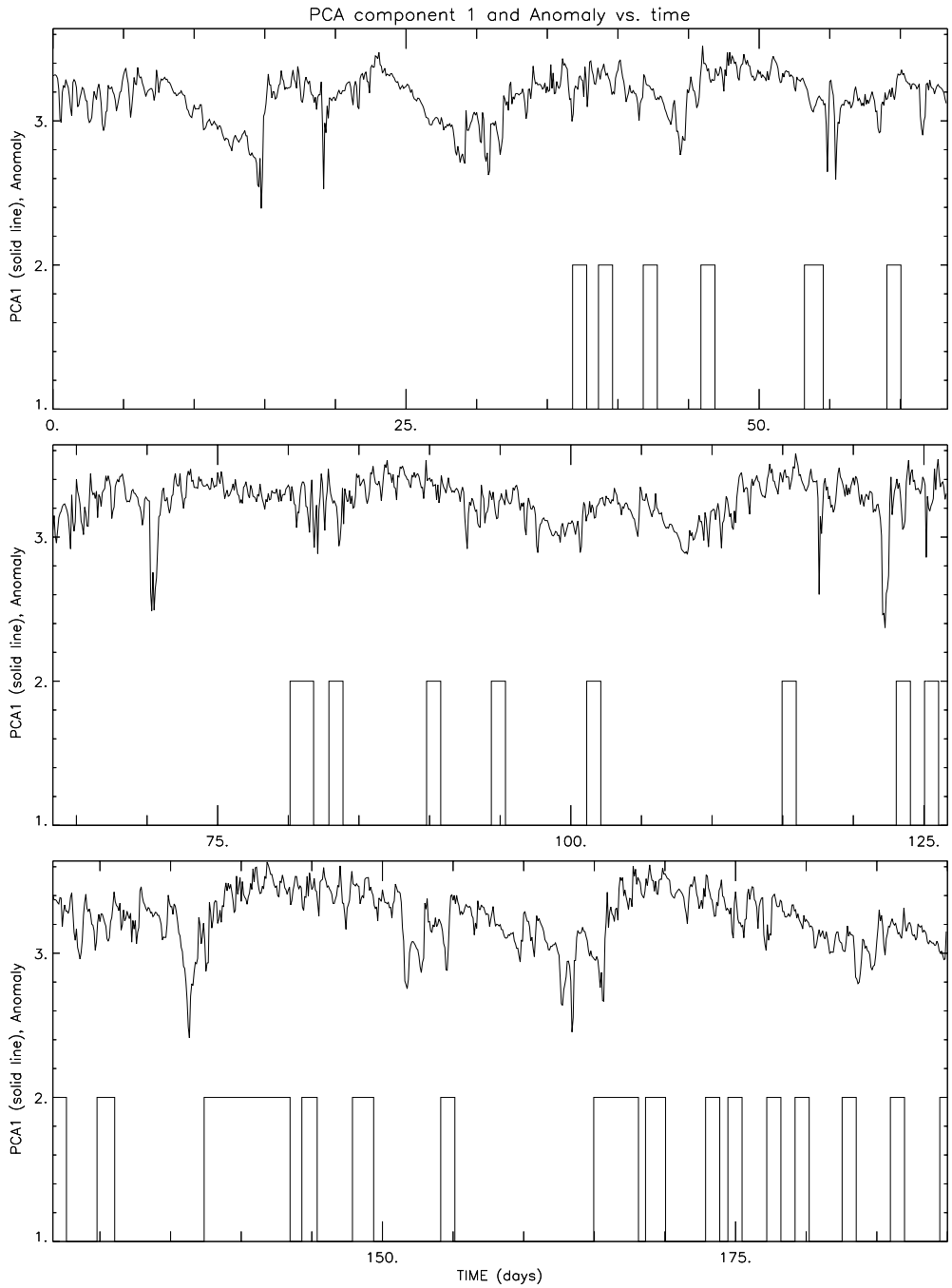

Fig 8. *The PCA1 plotted as function of time. The squared line indicates the time of an anomaly.*

The prediction (the output) of anomaly or non-anomaly can be represented differently. For instance only one type of anomaly could be used in training and testing a network, and/or the prediction resolution could vary. A one point (2 hour) prediction resolution means that if an anomaly occurs within 2 hours of the prediction, the output should be 1. If the prediction resolution is set to one day, 12 points (i.e., rows in the data file with 2-hour resolution) will indicate 1 if an anomaly occurs. Due to this is a desired output 1 referred in this report as a

warning, since one anomaly causes several output rows with 1's. As a further result, if two anomalies are closer than 12 points they will cause fewer than the expected 24 warnings. Depending on the result of the analysis one can change the criteria of the output data.

Table 4 *All the different combinations for the PCA file used in this report. The pa3 described in text.*

ref. name	point resolution	number of PCA used	total number of columns	length of time window (h)	
pa0	12	3 bin 0, 1, 2, 3, 4	15	24	original electron flux from the 5 used bins
p01	12	3 bin 0, 1	6	24	original electron flux from the 2 used bins
p02	12	3 bin3, 4	6	24	original electron flux from the 2 used bins
pa2	3	3	9	24	
pa3	12	3	9	48	described in text
pa4	3+12	6	18	48	points at 0, 4, 7, 10, 12, and 48
pa5	3	4	12	20	
pa6	6	6	18	54	
pa7	12	6	18	144	

4.3 Neural network analysis

A program was written to combine the seven different time periods into one large data file. The treatment of the data files as input to the different neural networks is described in Appendix 1. The data file consists of one of the files from Table 4 containing the PCA information, the frequency analysis and the desired output. The final file contains about 27.600 2-hour intervals, i.e. about 2.300 days or 6.3 years of data. The number of anomalies is about 522. If the data file is built to predict an anomaly within 24 hours, the data file (27.600 rows) will contain 20% of lines with warnings.

The first test of the data using a neural network with a back-propagation learning algorithm is displayed in Table 5. PE indicates the numbers of layers and number of neurons in them. The prediction resolution is noted "p" (1p means prediction within 2 hours). In Table 5 the PCA combination "pa3" is combined with a frequency analysis (wa*) which gives the size of the net 24+1 (24 inputs and one output). The output of the trained net is a decimal number and a threshold value has to be chosen to get the best result. In Table 5 the success of the different nets are calculated from a threshold of 0.5. In Table 6 a case from Table 5, row number 3 has been further studied with different net sizes. When the threshold was set so that about 85-90 % of the non-anomalies were predicted 40-45 % of the anomalies were correctly predicted, more or less independent of what we did with the data.

From the cases in Table 5 the prediction success of anomalies at different local times are analysed. When this type of check is made, a warning is counted in the local time sector where the associated anomaly occurred. In this way a prediction resolution of 12 points will not lead to an evenly spread number of warnings in each local time sector.

Table 5. *Prediction of anomalies within 2 or 24 hours using all anomalies. PE is the number of neurons in each layer, p the number of points to predict within (2 or 24 hours prediction), wavelet time window. The success rate for each case is expressed as percentages of each category. The threshold level on the output from the back propagation is set to 0.5.*

File type			**Training set**	**Training set**	**Test set**	**Test set**
PE	**p**	**data combination**	**anomaly (%)**	**non-anomaly (%)**	**anomaly (%)**	**non-anomaly (%)**
10	12	wa 64[0]	38	88	37	88
10+4	12	wa 64[0]	38	89	36	89
10+4	1	wa 64[0]	45	93	44	86
10+4	1	wa 32[0]	45	91	49	88
10+4	1	wa 128[0]	47	89	44	86
10+4	1	wa 64[0,1]	53	88	39	84
10+4	1	wa 32[2]	44	88	44	88
10+4	1	wa 32[3]	42	89	49	87

0) Using _all

1) Selected number of anomalies (only type 1, 2, 3, 6, 7, 10, and 13)

2) Using _high

3) Using _low

Table 6. *From Table 5 case row 3 in more detail with different numbers of neurons and layers (PE). (pa, 3 wa64, 1point)*

	Train	**Train**	**Test**	**Test**
PE	**anomaly**	**non-anomaly**	**anomaly**	**non-anomaly**
6	46	91	47	83
3	47	90	48	82
3+3	47	90	41	87
6+3	48	89	49	80
24+8			43	84
80			40	88

In Table 7 the prediction rates for local time sectors from 2-24 hour local time are given. There are more anomalies in the morning sector (Figure 4). The success rate (percentage) is higher in the same sector.

In Section 4.1 the information from the SEM-2 instrument has been pre-processed so less input data are used. The pre-processing of the data is done in such way that the largest variance of SEM-2 measurements is used without introducing the information from the anomalies. The many-dimensional problem is transformed down to three dimensions with the PCA analysis. The data files are then a combination of the PCA results and the dynamics of the largest coordinate from the PCA analysis through a frequency analysis (wavelet transformation). No information of time (i.e. year, month or time of day) is used in the input data. The output, i.e. warning or not, can be selected from different criteria. With this we can predict about 50% of the anomalies. Different network sizes and combinations of the data are made with only small changes of the result.

Table 7. *Success rate depending on position in orbit.*

			1	**2**	**3**	**4**	**5**	**6**	**7**	**8**	**9**	**10**	**11**
DATA _all pa3	**PE**	**point**											
wa64	10	6	52	44	35	49	33	33	33	29	35	36	33
wa64	10+4	12	51	44	35	49	32	30	33	27	33	35	33
wa64	10+4	1	70	66	53	61	35	21	36	16	17	29	34
wa32	10+4	1	65	68	45	60	30	24	38	29	31	47	44
wa128	10+4	1	66	58	45	47	36	26	39	33	32	50	52
wa64 [1)]	10+4	1	61	57	55	52	40	32	36	41	31	42	46
wa32 [2)]		1	65	50	47	65	36	41	38	29	31	29	30
wa32 [3)]		1	61	58	50	55	39	26	35	34	26	37	44

1) Selective number of anomalies (only type 1, 2, 3, 6, 7, 10, and 13)

2) Using _high

3) Using _low

4.4 Two classes of anomalies

From Section 4.3 the dependence on different input and network configurations is seen to be not that large. No selection criteria are found with the help of LT or anomaly type separation. This indicates that either we have different processes that the network cannot separate or some of the anomalies have a cause, which is not introduced into the input data files.

In order to find the different processes a closer investigation of the PCA was made. No clear correlation was found during times when the PCA1 started to vary. No correlation was found with the low fluxes of the PCA1 component. But after a closer inspection it was found that after a high PCA1 value it was 70% certain that an anomaly would occur. This led to a further investigation of what a high value of PCA1 indicated. How good indicator is this to predict anomalies?

Table 8 shows the success using a high value of PCA1 as a tool for warning. In the table all three data files are used (_all, _high and _low). The level was calculated as percentages of the maximum value of PCA1 (different maximum for each data file). The level was set to

optimise the result. Depending on the level value the number of high values (column 3) will be different and hence the success of the warning system (column 7 and 8). From the presented combinations the probability that an anomaly will occur after a high value is high (60-78%). Comparing the prediction resolution (1 and 12 point) the anomaly often occurs less than 24 hours after a high value. The success rate is comparable to the success of the earlier trained net (Table 4). The number of anomalies is predicted with 41% success (compared with the total number of warnings 31%) when the prediction for non-anomalies is at 84-86%.

Table 8. *The efficiency of using a high value of PCA1 as an indicator of anomalies. One high value of PCA1 (high electron flux) is used to warn for anomalies within the next 24 hours. Three cases, one from each data file (_all, _high and _low) are presented. The maximum of the PCA1 is found in column 1 together with the level used. The prediction resolution here is how many warnings are using the electron threshold as an indicator. High values are the total number of cases found above the level, and the number of associated points is the number of periods with high risk. Then follows how many of the high values are followed by an anomaly or not. The last two columns show the success of this prediction method.*

27391 points	**prediction resolution**	**high values**	**assoc. high points**	**high value followed by true warning**	**high value not followed**	**anomalies found**	**non-anomalies found**
				12 points	12 points		
_low lev.95 max2.204	1 point	730	3980	60% (439)	40% (291)	41% (237)	86%
_low lev.95 max2.204	12 point	730	3980	71% (519)	29% (211)	31% (1618)	84%
_high lev.94 max1.506	1 point	251	1341	78% (196)	22% (55)	23% (131)	96%
_high lev.94 max1.506	12 point	251	1341	84% (213)	15% (38)	15% (773)	97%
_all lev.95 max3.68	1 point	377	1941	75% (281)	25% (96)	29% (167)	93%
_all lev.95 max3.68	12 point	377	1941	83% (313)	17% (64)	20% (1038)	96%

The anomaly set was then divided into two groups; filter I (fI) and filter II (fII). Filter I contains warnings following a high value of PCA1. The level is selected so that about 1/5 of the warnings exist in the group of filter I. The warnings in filter II are the remainder (anomaly not clearly associated with high fluxes). In Table 9 a number of tests with different data combinations, levels and neural net sizes have been made. For each test of a combination three different training sets are tested (_all, _high, and _low). First the net is trained with all anomalies and tested both with the test set and then with the full data set in a time series (see Appendix). Secondly the net is trained with the case associated with high-flux-warnings and finally the net is trained with the warnings not associated with the high fluxes. In each square in Table 9 up to four percentages values are written; the top row is the success of the anomalies and the bottom is the success of the non-anomaly. Since the network gives a decimal output, the threshold of interpreting the output as warning or not warning can be set

to any value. We present in Table 9 one or two different results depending on the selected threshold. The threshold is selected in such way that the success rate on non-anomaly is close to or above 80%.

Table 9. *Test runs for the prediction of anomalies on Meteosat-3. The All anomaly filter I and filter II are the selection of the training data set (2/3 of all anomalies, 2/3 of the anomalies associated with high fluxes or 2/3 of the anomalies not associated with the high fluxes). The test column is when the net is tested with the remaining 1/3. The column time series is when all anomalies and all non-anomalies (approximately 27516 points) have been tested on the net. Since the output from the net is a decimal number and this can be chosen differently we present the results from one or two thresholds, selected close to or above 80% success for the non-anomalies. The top row is for the success of the anomalies and the bottom the success of the non-anomalies. The different rows are codes as follows: first the input data source then whether data are based on _all, _high or _low. Level is the level used to divide the anomalies in filter I & II depending on the _all, _high and _low files. Net is how many inputs + outputs are used for each case. And finally PE is the number of neurons and layers in the tested back propagation network.*

	Meteosat 3	**Settings**	**All anom.**		**filterI**		**filterII**	
	Data	**level net PE**	**test**	**time series**	**test**	**time series**	**test**	**time series**
1	pa3 _all	0.96 9+1 6+2	57 41 77 88	56 40 77 88	94 94	26 94	25 50 88 72	32 59 91 73
2	wa64 _all	0.96 15+1 8+3	40 23 77 91	39 22 79 91	61 86	34 21 83 92	30 8 82 96	33 11 83 96
3	pa6 _low	0.96 18+1 9+3	46 32 81 91	48 33 81 91	82 89	39 27 87 93	27 7 82 97	25 7 83 96
4	pa6 _low	0.95 18+1 9+3			71 91	41 28 86 93	32 7 76 96	27 7 77 96
5	pa5 _high	0.93 18+1 9+4	48 30 79 91	51 32 78 91	83 93	35 28 88 92	37 17 80 94	35 16 80 95
6	pa5 _all	0.95 18+1 9+3	47 31 79 90	50 34 79 90	92 92	32 28 88 91	36 3 88 96	42 14 80 95
7	pa6 wa64 _all	0.96 33+1 16+8	63 43 66 80	62 44 68 83			43 27 75 87	43 27 76 89
8	pa7 wa128 _all	0.95 33+1 10+6	52 35 76 88	53 38 76 87	92 91	32 28 89 91	37 20 79 92	39 20 80 92
9	pa3 wa32 _all	0.95 24+1 10+6	51 37 78 89	52 38 77 88	92 92	34 30 90 92	42 23 75 89	42 24 77 90
10	pa3 wat32 _all	0.95 24+1 8+4	53 37 76 88	54 39 76 87	93 91	36 30 88 91	39 21 76 91	42 20 87 92
11	pa3 wa32 _all	0.95 24+1 5+2	53 37 75 88	54 38 75 88	92 92	34 28 89 92	41 21 75 91	44 22 78 92
12	pa3 wa32 _all	0.94 24+1 5+2			87 89	34 30 89 91	38 16 79 93	36 16 78 94

13	pa3 _all	0.95 9+1 5+2	48 32 80 91	48 32 78 91	91 92	34 23 87 93	38 17 77 95	36 14 79 95
14	pa6 _all	0.95 18+1 5+2	53 35 78 90	54 36 76 89	92 89	31 26 91 93	43 18 76 93	39 17 78 93
15	pa6 _all	0.95 18+1 5+2	50 33 80 91	50 33 78 91	93 91	28 24 91 94	41 16 79 94	38 15 79 94
16	pa3 _all	0.95 12+1 5+2	51 30 78 91	52 31 76 91	90 91	26 23 92 94	45 16 77 95	35 16 78 95
17	pa2 _all	0.95 9+1 5+2	51 28 77 92	52 29 77 92	94 87	30 25 89 92	42 11 77 97	36 10 77 96
18	pa2 _all	0.95 9+1 8	55 31 74 91		89 91		36 7 78 97	
19	.pa0	0.95 15+1 5+2	44 21 78 93	46 22 79 93				
20	.p01	0.95 15+1 5+2	40 23 81 92	42 25 81 25				
21	.p02	0.95 15+1 5+2	41 19 82 94	43 19 80 94				
22	pa3+month [12]	0.95 10+1 5+2	50 31 79 92	51 32 78 91				
23	pa3+month [6]	0.95 10+1 5+2	56 32 79 92	51 33 78 91				
25	pa3+year	0.95 10+1 5+2		51 34 82 92				
25	pa3+hour	0.95 10+1 5+2	71 49 56 80	50 29 78 92				
26	pa6_all	0.95 18+1. 5+2	67 49 63 81	69 50 61 79	93 90	27 45 91 80	37 16 80 94	39 17 82 95

[12] The year divided from 1 to 12.

[6] The year divided from 1-6,1-6 with the equinox centred.

The separation of anomalies into warnings associated with high or low fluxes of electrons introduces no new information to the prediction (rows 1-18). If we calculate how many warnings the net trained with all predicted anomalies and compare that with how many anomalies are predicted with filterI and filterII together the result is almost equal. In filterII anomalies that were associated with high fluxes were removed, but predicted anomalies linked to high-flux, i.e. a failure to train a net to find another source to the anomalies than high fluxes of electrons. The models can only find the warnings that are associated with the high fluxes.

In Table 9 tests have been done with only a combination of the PCA results (files described in Table 4) row 1, 6, etc. In row 2 only data from the frequency analysis is used. The prediction success rate using only the combination of the PCA is higher than only using the frequency analysis. If one adds the two parts (row 7, 11 etc.) we do not get any significantly higher success rates. A comparison between the _high (high energy) and the _low (low energy) is made in row 3-5 and then compared with row 6. There are no significant changes of the prediction rate. At row 13-18 different combinations of PCA (see Table 4) did not improve

the result. Consequently only three points of the PCA is enough to make the prediction. More points or dynamics (frequency analysis) will not increase the prediction success significantly.

If one compares Table 9 with a linear combination of the high flux of PCA alone, a trained net prediction of the warnings to 43% and has success with 53% of all anomalies when 84 % of non-anomalies are correctly predicted. (For high flux alone the values were 31 % of the warnings or 41 % of the anomalies when 84 % of the non-anomalies are correctly predicted).

In Table 10 and 11 the prediction success rates for the different local times and anomaly types are presented. As in Table 9 the net is trained on three different files, all the warnings (me), only warnings associated with high fluxes (fI) and finally the rest of the warnings (fII). The tested data file is the full time series, the prediction resolution 12 point (24 hours) or 1 point prediction resolution. The test with the prediction resolution of 1 point shows how many of the anomalies are predicted and compare with the 12 point prediction resolution when warnings can be shared with other anomalies. For filterII (fII) the threshold 0.5 is usually a little too high, with a threshold 0.4 the success rate is higher.

Table 10. *The prediction success rate for different anomaly types as function of the local time. See the text of Table 11 for more information on nomenclature.*

threshold 0.5												
Local time	**0-2**	**2-4**	**4-6**	**6-8**	**8-10**	**10-12**	**12-14**	**14-16**	**16-18**	**18-20**	**20-22**	**22-0**
All anom.												
12 point	435	551	556	509	526	393	336	327	342	348	367	489
1 point	50	64	61	60	62	44	34	33	37	35	39	51
me-me-12	21	47	35	29	35	21	20	25	20	23	22	19
me-me-1	36	69	57	50	48	27	18	36	24	20	28	33
fI-me-12	17	38	31	30	26	23	20	19	19	26	20	18
fI-me-1	24	50	48	47	47	32	26	30	24	26	26	27
fII-me-12	14	18	20	8	16	5	4	10	2	9	8	10
fII-me-1	24	25	26	13	15	7	3	15	5	6	13	18
only A												
12 point	332	481	491	414	437	276	234	254	293	265	303	398
me-me-12	21	47	35	29	35	21	20	25	20	23	22	19
fI-me-12		40	32	29	22	27	21	18	18	27	19	17
fII-me-12		28	26	16	23	12	6	18	6	12	14	13
only B												
12 point	103	70	65	95	89	117	102	73	49	83	64	91
me-me-12	9	21	11	12	13	7	3	0	4	4	9	7
fI-me-12	13	46	23	19	38	7	16	12	18	0	0	0
fII-me-12	2	0	0	2	1	1	2	0	0	0	0	1
only C												
me-me-12	40	68	52	48	50	45	28	46	41	31	37	29
fI-me-12	22	46	35	32	27	30	17	23	23	27	17	18
fII-me-12	32	30	28	24	38	28	17	28	17	14	25	26

From Table 10 it can be seen that the best prediction is made in the local time sector 2-10 LT (as was found in Table 7). The number of correct warnings is up to twice the success rates at other local times. Most anomalies occur at these local times (Figure 4 and Section 4.2.3). If one remove the predicted warnings, the number of unpredicted warnings in each LT sector is fairly constant. There is a slight difference with fewer missed warnings between 10-22 LT.

Table 11. *The prediction success for the different codes with a threshold level of 0.5 (this is high specially for filterII see Table 9). The table gives information on the number of warnings for 1 point (within 2-hour warning) and number of warnings for 12 point (within 24-hour warning). The first letter gives information on the trained anomaly set: m used the full anomaly set (2/3 train 1/3 test), I filter I (2/3 train 1/3 test) and II filter II (2/3 train 1/3 test). The numbers 1 and 12 show how long beforehand the net should predict an anomaly (within 2 or 24 hours). For "all anom" all anomalies are used, "sort A" only anomalies with code 1, 2, 3, 5, 6, 7 and 9 (anomalies that have a high occurrence rate), "sort B" only anomalies with code 4, 8, 10, 11, 12, 13, 14, 15, 16, 17 and 18 (anomalies with low occurrence rate) and "sort C" anomalies with code 1 and 3 (anomalies with high success rate from sort A).*

level .5																		
Code	**1**	**2**	**3**	**4**	**5**	**6**	**7**	**8**	**9**	**10**	**11**	**12**	**13**	**14**	**15**	**16**	**17**	**18**
12 point warnings	2247	556	837	1	47	294	134	45	63	441	12	105	228	43	16	24	11	75
1 point warnings	246	59	100	1	5	32	12	4	7	53	1	9	23	5	2	2	2	7
all anom																		
m-m-12	34	10	35	0	28	21	30	20	19	23	0	10	21	0	75	13	0	0
m-m-1	47	19	54	0	60	28	42	0	43	36	0	22	35	0	50	50	0	0
I-m-12	29	6	28	0	26	37	30	4	5	23	0	11	27	0	75	8	0	0
I-m-1	41	14	43	0	40	41	42	0	29	36	0	11	35	0	50	50	0	0
II-m-12	14	8	16	100	6	4	14	9	21	7	0	0	2	0	0	4	0	0
II-m-1	18	12	24	100	20	13	8	0	29	6	0	0	0	0	0	50	0	0
sort A																		
m-m-12	37	11	38		28	23	29		24									
I-m-12	28	6	27		28	36	30		8									
II-m-12	20	11	20		15	6	17		22									
sort B																		
m-m-12				0				2		11	0	1	9	9	50	0	0	0
I-m-12				0				24		23	0	14	24	5	75	4	0	0
II-m-12				0				0		1	0	0	1	2	0	0	0	0
sort C																		
m-m12	45		43															
I-m-12	27		28															
II-m-12	26		26															

In Table 11 the result is presented when studying the separate anomaly types (Table 2). The radiometer stops (code 1 and 3) seem to be associated with high fluxes of electrons. It is possible to predict the anomalies associated with the battery charger (code 5, 6 and 7) and SIC

(code 13) anomaly. The corrupted/lost image lines (code 10) that occur mainly at the end of the mission are also predictable. The other anomalies are not so easily predicted or the poor statistics is not able to give significant results.

Table 12. *The possibilities of predicting the individual types of anomalies. Data used are pa3 _all with 9 inputs (net9+1) and two layers of back-propagation (PE5+2). Each type of anomaly has been trained and tested individually except anomalies with low frequency of occurrence (marked * in table). They have been analysed together (see code 4). First column is the code, second column number of total warnings, success rate for the test file (for two different thresholds, top anomaly, bottom non-anomaly), third column test of success with full time range (success of anomaly only, threshold 0.5). The last twelve columns describe the result for the local time (2-hour resolution). The top value is the total number of cases in the local time sector and the bottom is the success in percentages.*

	number	**Test**	**Sort**	**1**	**2**	**3**	**4**	**5**	**6**	**7**	**8**	**9**	**10**	**11**	**12**
1	2247	36 55 89 79	39	138 43	178 61	303 50	280 38	277 44	169 34	121 31	153 42	186 27	115 37	140 26	187 24
2	556	09 28 97 81	11	58 21	72 8	97 5	18 0	52 11	26 0	20 0	24 0	25 92	61 18	67 0	36 0
3	837	28 50 92 78	30	133 35	138 44	80 30	67 28	46 41	45 33	57 11	51 20	24 25	25 0	29 34	142 21
4	* 1	30 56 83 73	41	28 21	66 50	20 15	22 59	24 42	24 13	48 31	12 83	24 50	29 31	16 56	24 67
5	* 49														
6	294	38 75 88 77	41	0 0	29 48	0 0	37 43	38 37	24 0	12 17	14 64	22 73	40 28	45 42	33 58
7	134	73 80 79 75	82	0 0	32 63	0 0	12 83	12 83	12 92	12 83	0 0	24 83	12 100	18 94	0 0
8	* 45														
9	* 63														
10	441		84	30 83	18 56	45 80	37 81	52 92	45 87	32 84	46 74	37 76	42 95	38 89	19 95
11	* 12														
12	105	46 32 78 82	67	24 75	12 50	11 82	12 92	0 0	12 42	10 60	0 0	0 0	0 0	0 0	24 63
13	228	40 56 80 72	45	24 0	6 100	0 0	24 50	25 100	36 33	24 58	27 59	0 0	24 17	14 86	24 4
14	* 43														
15	* 16														
16	* 24														
17	* 11														
18	* 75														

* The number of all these different types is 337. The result of the run in row code 4.

The purpose of the PCA transformation was partly chosen to reduce the number of inputs. The result of Table 9 row 1-18 is that only 3 points of the PCA are needed to make the prediction. In addition the PCA originates from the electron fluxes of the SEM instrument. A test using the five energy bins with 3 different points to predict the anomalies was made. The

data file was set up as described in Table 5 row 1 and the result is given in Table 9 row 19. The statistical result is 10% worse than the PCA runs. The output of the model using PCA and the model using electron flux are different. The PCA analysis removes some of the large variation in the daily data, therefore the output signal from the PCA prediction is easier to interpret. In row 20 and 21 (Table 9) only the low energy and the high-energy bins are used (see Table 4 row 2 and 3). The result is the same as using the five energy bins and there is no clear difference between the low and the high bins.

Up until now the input data have not contained any time information. In row 22-25 Table 9 time has been introduced as input information. Information of the month, the equinox asymmetry is expected to improve the prediction (Figure 4). In row 22 the time is represented as the month of the year (decimal value). No improvements on the predictions were made so instead of 12 months, the time was selected to run only 6 months (half year) and shifted some days to get the equinox in the centre of the time period. This did not help either. The difference between different months (Figure 4) is already found in the information of the electron fluxes.

The local time dependence has been stressed throughout this report. In row 25 Table 9 the prediction is made with help of the time of the day (UT). This does not lead to any higher prediction rate; the variation of the fluxes seems to be sufficient.

For the anomalies we can see a change with time. The effect of ageing helps the network if the year is added as information. Again according to row 25 Table 9 there are no improvements.

As tested in Table 11 there is a difference in the prediction rate of the different anomaly types. A new test was done but now the train and test sets are made up of only one type of anomaly (Table 12). The anomaly types, which have a low occurrence rate (code 4, 5, 8, 9, 11, 14, 15, 16, 17, and 18), are combined as one anomaly code to get sufficient statistics. In Table 12 the total number of warnings for each anomaly type are presented in column 2. The result of the test file is represented in column 3 in the same way that the result is presented in Table 9. Column 4 is the prediction result for all the anomalies of the type with a threshold of 0.5. The last 12 columns show the prediction result divided up into local time sectors. For each local time the warning rate is associated to that sector and the success rate is presented as a percentage. For code 12 the prediction rate from the test file is 46% if the non-anomalies are allowed as low as 78%. Statistically this is 48 of the warnings that should be predicted out of 105. But when we test the net on the total number of points (about 27391) the result can not be used. Due to the variety of different environment conditions in the training net for the warnings and the low number of cases in the training set (about 70 anomalies and 140 non-anomalies) the net is not consistent. The predicted output in the test run with the continuous time series fluctuates constantly between 0 and 1. The result of the run is more luck than a trained prediction. For the anomalies code 13 the environment at the time of anomaly is more homogenous using the test run with the continuous time series even though the statistical result was worse (40% of the anomalies and 80% of the non-anomalies predicted).

The result is that if the number of events for this type of complex problem is low the result might not be good. Only if one makes a continuous time series and tests the net on the time serie the quality of the prediction can be evaluated. It is not sufficient only to present the statistical success of the prediction rates. In earlier studies the test of a continuous time series

has not been used and the focus has been on the radiometer anomalies (code 1, 2, 3, 4). In this report (Table 12) the success rate between the three types of anomalies is different. The radiometer position jump (code 2) is hardly predicted at all while almost half of the radiometer stops (code 1) and the radiometer position jump and stop (code 3) are predicted much better. It might be that the stops are associated with high electron fluxes and jump is caused by something else.

To separate the warnings associated with high fluxes did not give much better results. No clear correlation with LT or anomaly type was found. The introduction of PCA analysis improved the prediction rate and the analysis of the output (the prediction will not vary so much between two prediction points). No clear difference between the low and the high-energy range was seen. The information of time exists already in the electron fluxes (as much as is needed). The anomalies were separated in order to find other causes than high-energy fluxes but this failed. Other types of information have to be introduced to the input to obtain a better result. If one removes the predicted anomalies the unpredicted anomalies are evenly distributed in local time. A high value of PCA1 (see Table 4 for levels) is followed with 60-78% certainty by one or more anomalies within 1 day. With this prediction, up to 41% of the anomalies are predicted. The non-anomaly is still predicted with high accuracy (84-86%). An on-board monitor detecting high fluxes can automatically give a correct warning for up to 41% of the anomalies that occurred on Meteosat-3.

4.5 Prediction possibilities using neural networks

Separating the warnings with the high fluxes did not improve the prediction rate significantly. The use of a high value as the warning signal is not preferable since most of the warnings are made less than 24 hours in advance. If one wishes to use the SEM-2 fluxes for prediction in real time, the clearest output signal is found when the neural net is trained only with warnings associated with high fluxes. In Figure 9 a period of time is presented. The result in the figure is from the run presented in Table 9 row 26. The lines in the continuous time sequence are from top to bottom: the Dst, the result of training with all anomalies, the result of training with only the anomalies not associated with high fluxes, the result of training with the anomalies associated with the high fluxes and finally the Kp index. The squared line in the three middle lines indicates when an anomaly occurred. They are 12 points long or longer indicating the resolution of the prediction (within 24-hour warning). If one allows a success rate of predicting the non-anomalies of 80% the warnings can be predicted to 47% (this will be about 57% of the total anomalies) for the net trained on the high fluxes. If one compare the three results from each net (line 2, 3 and 4), the line 2 (trained on all anomalies) is more or less the sum of lines 3 and 4. The net trained with the anomalies associated with high fluxes is the output that is easiest for an operator to use. The net trained on anomalies not associated with high fluxes (line 3) is better at predicting the start of a period of high fluxes.

From comparing the predicted value and Dst we can see that the resemblance is not very good. One conclusion is that when Dst drops drastically (a magnetic storm) the prediction for the anomalies also drops. If one then compares the prediction result with Kp there is a much better correlation. The output from the net trained with all the anomalies (line 2) fluctuates almost as much as Kp (line 5). This should not be surprising since the Kp index is calculated from information on high latitude magnetometers, almost the same magnetic field lines as the GEO. The Dst on the other hand is calculated from measurements from closer to the equator and does not always clearly display substorm activity occurring on field lines connected to higher latitudes.

Since the probability of predicting anomalies seems to be associated with increased fluxes of electrons, the result from analysing the time series at solar minimum shows a clearer picture. At solar minimum the storms are more regular and separated, and hence the net works better at the end.

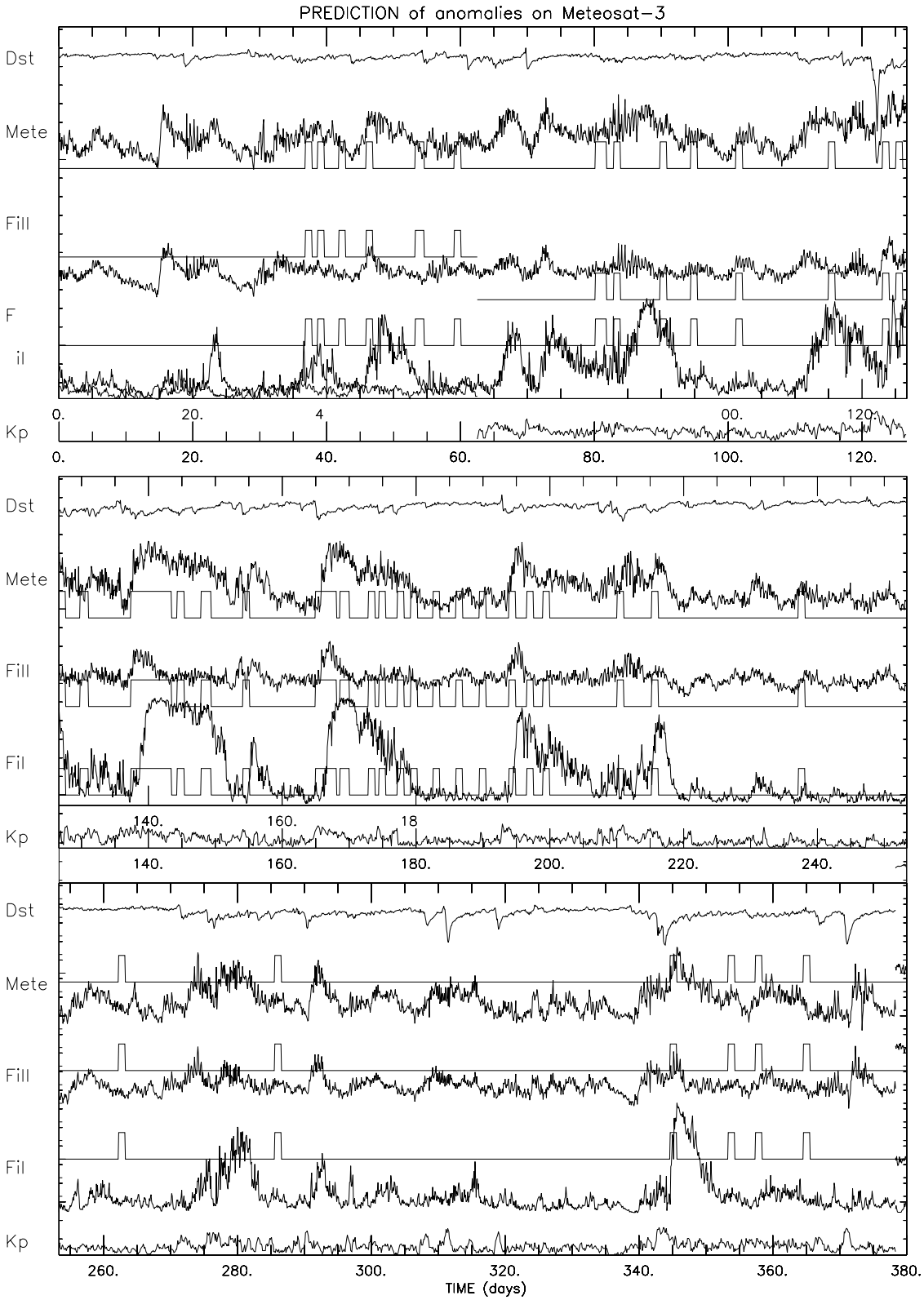

Fig 9. *The predicted result from three different trained nets. The result and the configuration of each net are presented in Table 9 row 26. The second line is the result of training the net with all anomalies. The third line is a net trained with filter II and fourth line is for a net trained with filterI. The lines one and five are Dst and Kp respectively. The squared line indicates all the warnings.*

5 Summary and conclusions

The Meteosat-3 has an environment monitor (SEM-2) mounted on board. In this study the information from the SEM-2 has been used to predict the anomalies that occurred on Meteosat-3 during the mission.

SEM-2 monitored the electron fluxes in five energy ranges from 43-300 keV. The mission started in June 1988 and continued for about seven years. During this time Meteosat-3 had on the average anomalies during 20% of the days.

When analysing on-board measurements of electrons the time resolution must be better than 24 hours because the natural variation of the electron fluxes is larger than the difference between anomaly and non-anomaly conditions.

In order to keep the number of inputs into the prediction model as low as possible a PCA analysis was performed on the measured electron fluxes. When using only the largest component from the PCA analysis 41% of anomalies can be predicted. The probability that a high value of the PCA first component will be followed by an anomaly within 24 hours is 60-78%. The non-anomalies are correctly predicted to 84-86%.

The result from neural network prediction 24 hours ahead was that 43% of the warnings (i.e. 53% of the anomalies) were predicted when 84 % of the non-anomalies are correctly predicted. This is about 10% better than the method described above.

The predicted anomalies were associated with high flux of electrons and seem to be independent on energy level. Attempts to find other causes than high electron fluxes were made but failed using this data set. These data only give information about the flux of electrons in different energy bins. The study of the local time dependency and anomaly types did not improve the prediction.

Using the results of this study, one can conclude that an on-board monitor with relatively high temporal resolution combined with an automatic warning system could be based on information on high fluxes to be able to give a warning for at least the next 24-hour period. The warning system for a satellite operator can be based on the anomalies associated with the high electron fluxes (Figure 9 line 4). It is recommended that environment monitors always be included on-board spacecraft. Not only to make it possible to predict times of higher risk for

damage of components or system failures but also together with instruments on other spacecraft to produce a data base that can help us to understand the space environment and its effects better. Long time series of data will be needed in the near future to separate long-term effects from variations on shorter time-scales. This type of investigations can be compared to the importance of having long time series of ground temperature measurements to understand the climate changes on the Earth.

6 Acknowledgements

We wish to thank the ESA-TOS-EMA for initiating this project and their interest throughout its completion. Special thanks belong to the ESTEC Technical Officer Dr. Alain Hilgers and to Dr. Eamonn Daly whose comments and support were particularly useful.

7 References

Anselmo, J.C., Solar storm eyed as a satellite killer, Aviation week and Space Technology, January 27, 1997.

Baker, D.N., J.H. Allen, R.D. Belian, J.B. Blake, S.G. Kanekal, B. Klecker, R.P. Lepping, X. Li, R.A. Mewaldt, K. Ogilvie, T. Onsager, G.D. Reeves, G. Rostoker, R.B. Sheldon, H.J. Singer, H.E. Spence, and N. Turner, An assessment of space environmental conditions during the recent Anik E1 spacecraft operation failure, ISTP Newsletter, Vol 6, No. 2, June 1996.

Coates, A.J. , A.D. Johonstone, D.J. Rodgers, and G.L. Wrenn, Quest for the source of Meteosat anomalies, Proc. Spacecraft Charging Technology Conference 1989, Naval Postgraduate School, 120-146, 1991.

Fredrickson, A.R., Radiation induced dielectric charging, in “Space Systems and their interactions with the Earth's space environment,” Eds. Garett and Pile, Vol 71, 386-412, AIAA, Washington DC, 1980.

Frezet, M., E.J. Daly, J.P. Granger, and J. Hamelin, Assessment of electrostatic charging of satellites in the geostationary environment. ESA Journal Vol 13, 89-116, 1989.

Grystad, D., Meteosat operational anomalies correlation with the space environment, Design project report ESTEC, 1997.

Hoge, D., and D. Leverington, Investigation of electrostatic discharge phenomena on the Meteosat spacecraft, ESA Journal, 3, 101-113, 1979.

Hoge, D.G., Meteosat spacecraft charging investigation, ESA N82-14265, 1980.

Hoge, D.G., Results of Meteosat-F2 spacecraft charging monitors, in Proceedings of an International Symposium on Spacecraft Materials in space, ESA SP-178, 1982.

Klecker, B., Energetic particle environment in near-Earth orbit, Adv. Space Res., 17, (2)37-(2)45, 1996.

Kumar, P., and E. Foufoula-Georgiou, Wavelet analysis for geophysical applications. Rev. of Geophys., 35, 385-412, 1997.

Lanzerotti, L.J., C. Berglia, D.W. Maurer, G.K. Johnson III, and C.G. Maclennan, Studies of spacecraft charging on a geosynchronous telecommunications satellite, in Proceeding of the 1996 COSPAR conference.

López Honrubia, F.J., and A. Hilgers, Relationship between Meteosat time-tag anomalies and the high energy electron environment: A non-linear approach. Internal ESTEC working paper, no 1886, 1996.

López Honrubia, F.J., and A. Hilgers, Some correlation techniques for environmentally induced anomalies analysis. J. Spacecraft and Rocket, 670-674, 1997.

Rodgers, D.J., Correlation of METEOSAT-3 anomalies with data from the spacecraft environment monitor, Internal ESTEC working paper, no.1620, 1991.

Rodgers, D.J., A.J., Coates, A.D. Johnstone, and E.J. Daly, Correlation of METEOSAT-3 anomalies with data from the space environment monitor, in Proceedings of the ESA Workshop on Space Weather, WPP-ISS, Noordwijk, The Netherlands, 1999.

Vampola, A.L., Analysis of environmentally induced spacecraft anomalies, J. Spacecraft and Rockets, Vol 31, March-April, 1994.

Wilkinson, D.C., National Oceanic and Atmospheric Administration's spacecraft anomaly data base and examples of solar activity affecting spacecraft, J. Spacecraft and Rockets , Vol 31, March-April, 1994.

Wrenn, G.L., and A.J. Sims, Surface charging on spacecraft in geosynchronous orbit, in “The Behaviour of Systems in the Space Environment,” Eds. R.N. DeWitt et al., Kluwer Academic Publ., Netherlands, 491-511, 1993.

Appendix 1

Data processing

For all data files that have been used throughout this report the train and test files have been created in the same way. When using neural networks one needs to know their limitations. A neural net is mainly sensitive to the first two significant figures. If the data have a high dynamic range, over several orders of magnitude, the data have to be pre-processed. Taking the logarithm of the electron fluxes gives a smaller dynamic range and a more linear coverage between the minimum value and the maximum value. The neural net is built up so that the input values are between 0 and 1 or between -1 and 1 depending on the selected linear transform. The software that we have used was from NeuralWare. This software makes the normalisation and therefore the files used in this report are not normalised.

To make predictions two files are needed, a training set and a test set. After creating a data file where the columns represent the input into a prediction and the rows represent the different times (cases), the last column is the desired value (if anomaly occurred within the selected time window or not). If the desired value is 0 this indicates that no anomaly occurred within the resolution and if it is 1 an anomaly occurred. For the total time period with the data at a resolution of 2 hours (the rows in the files) there will be many more non-anomaly cases than anomaly cases. If the prediction is for an anomaly within 24 hours the data file will contain 20% anomalies and 80% non-anomalies. If a net is trained with this relation it would be good at predicting non-anomalies. The relation between the two categories should be more like 1:1. A net that will cause too many false warnings would not be useful, so there are more non-anomalies than anomalies used. Throughout the report twice as many non-anomalies as anomalies have been used in the training and test files. All the selected anomaly/warning cases and twice the number of randomly selected non-anomalies are used to create one training and one test file. If only one anomaly type is analysed, all the other types of anomalies will exist in the non-anomaly category and the random selection can select them to represent a time with non-anomaly. The anomaly and the non-anomaly cases are randomly divided, 2/3 to a training set and 1/3 into a test set.

In the example of 24-hour prediction about 80% of the non-anomalies are not used in the training or the test set and could be added to the test set. Instead, an extra testing file was created consisting of all the cases in time order. This test file gives us information about the success of the non-anomaly prediction and how the prediction will look like in real time. By comparing the output from the time series test file, we can gain a good understanding of the usefulness of the net.

The output from the neural network is a decimal value. When the net is trained, a threshold needs to be set to separate when the network predicts anomaly or non-anomaly. In this report the threshold is selected so that the non-anomaly is predicted around 80% or better. This is equal to a false warning every fifth day.

The anomalies that are detected occurred at a given time. The data set that is created (description in Section 4) has a resolution of 2 hours. The desired output from our net will produce a prediction of whether an anomaly will occur within a time period. If the data set is

to predict anomalies within 24 hours, an anomaly will cause 12 rows (if they are in time sequence) to indicate an anomaly. If two anomalies occur closer than 24 hours apart they will create fewer than 24 rows of ones. As a result the number of ones in a created data file is not equal to the number of anomalies (times the resolution of the prediction). At the times when we can predict anomalies, more anomalies than one can occur in 24 hours.

A back propagation learning algorithm is used to train the neural network. Other networks can improve the result, but the highest possibility of getting a network to converge is with a back propagation network.

Analysis tools and theories

Principal component analysis, PCA, is a linear projection of multivariable data. The variables have to be correlated or else the PCA is meaningless. The new set of variables, the PCs, is linear combinations of the original variables. The largest variance is the first direction PCA1. The PCA2 is then orthogonal to PCA1 and the direction is defined by the direction of largest variance perpendicular to the first direction. That is, each PCA is derived in decreasing order of importance (Waldemark, 1996).

The method originates from the eigenvector analysis. Let x be an eigenvector of size N to a linear operator **A** (an N x M matrix). This is

$$\mathbf{A}x = \lambda x$$

where λ is the eigenvalue to the linear operator **A** and its eigenvector x.

To get the maximum variance in PCA1 the eigenvalues are sorted in decreasing order

$\lambda_1 > \lambda_2 > .... > \lambda_N$, where the eigenvalue λ_1 corresponds to PCA1.

All diagonal terms are equal to one in the correlation matrix. Thus, the sum of the diagonal terms will be equal to N (the diagonal sum is equal to the sum of the variance of the standardised variables). This gives that

$$\Sigma\lambda_i = N$$

and the percentage of the total variance that each PC explains is simply λ_i / N

Software for neural networks

The prediction model is made with a commercial package, Neural Works Professional II Plus (Neural Computing, 1996). This package gives the user a possibility to test different networks and improve the efficiency of the tested network. It also produces C-code for the trained network so one can transfer the network to another platform.

The neural network needs only a linear data file for analysis. The network itself normalises the data from the file, minimum and maximum values or by a users selection. Transformation functions and learning rules can be selected.

The program offers selection of different network types. In this work the classic back-propagation network has been used.

The number of layers and neurons are easy to change. Different momentum and learning coefficients can be used during iteration.

References

Neural Computing. A technology handbook for professional II/PLUS and NeuralWorks Explorer. NeuralWare, Inc. USA, 1996.

Waldemark, J., Investigation of suitable computer intelligence methods for automated analysis of multivariable satellite data, IRF Scientific Report 232, Kiruna, 1996.

Institutet för rymdfysik

Swedish Institute of Space Physics

Swedish Institute of Space Physics
Box 812, SE- 981 28 Kiruna, SWEDEN
tel. +46-980-790 00, fax +46-980-790 50, e-post: irf@irf.se

www.irf.se